

Stable Seamless Interfaces and Rapid Ionic Conductivity of Ca–CeO₂/LiTFSI/PEO Composite Electrolyte for High-Rate and High-Voltage All-Solid-State Battery

Hao Chen, David Adekoya, Luke Hencz, Jun Ma, Su Chen, Cheng Yan, Huijun Zhao, Guanglei Cui,* and Shanqing Zhang*

Stable and seamless interfaces among solid components in all-solid-state batteries (ASSBs) are crucial for high ionic conductivity and high rate performance. This can be achieved by the combination of functional inorganic material and flexible polymer solid electrolyte. In this work, a flexible all-solid-state composite electrolyte is synthesized based on oxygen-vacancy-rich Ca-doped CeO₂ (Ca–CeO₂) nanotube, lithium bis(trifluoromethanesulfonyl) imide (LiTFSI), and poly(ethylene oxide) (PEO), namely Ca–CeO₂/LiTFSI/PEO. Ca–CeO₂ nanotubes play a key role in enhancing the ionic conductivity and mechanical strength while the PEO offers flexibility and assures the stable seamless contact between the solid electrolyte and the electrodes in ASSBs. The as-prepared electrolyte exhibits high ionic conductivity of $1.3 \times 10^{-4} \text{ S cm}^{-1}$ at 60 °C, a high lithium ion transference number of 0.453, and high-voltage stability. More importantly, various electrochemical characterizations and density functional theory (DFT) calculations reveal that Ca–CeO₂ helps dissociate LiTFSI, produce free Li ions, and therefore enhance ionic conductivity. The ASSBs based on the as-prepared Ca–CeO₂/LiTFSI/PEO composite electrolyte deliver high-rate capability and high-voltage stability.

energy and power density and market ubiquity.^[1,2] Unfortunately, the liquid electrolytes inside traditional LIBs contain organic solvents that are usually flammable, corrosive, and thermally unstable, which could cause fire and explosion risks. With the adoption of flexible solid-state electrolytes (SSEs), all-solid-state batteries (ASSBs) can effectively alleviate these safety issues and boost the energy density by eliminating the flammable organic liquid electrolytes.^[3,4] Furthermore, the problems of short-circuits mainly triggered by Li dendrites in LIBs can be effectively suppressed in ASSBs. Additionally, flexible ASSBs can be bent, punched, or even pierced without safety concerns. Moreover, the high stability of SSEs can expand the electrochemical window, thereby improving the power density of ASSBs.^[5]

1. Introduction

Lithium ion batteries (LIBs) are one of the most promising energy storage devices in modern society due to their high


Generally, SSEs are divided into two major groups: polymer electrolytes and inorganic electrolytes.^[1] Inorganic electrolytes possess high ion conductivity and support battery operation across wide temperature ranges. However, metallic Li penetrating the inorganic bulk and unstable interface in inorganic electrolytes will trigger severe battery failure.^[6] Comparatively, polymer electrolytes have some complementary merits, such as transparency, lightweight, flexibility, thin-film forming ability, and easy processability, making them outstanding in ASSBs.^[7] Since the numerous pioneering works in the past decades, tremendous achievements have been made in significantly improving the performance of polymeric ASSBs. Typically, an ideal polymer SSE should meet some specific requirements, such as high ionic conductivity (comparable with liquid electrolytes), high lithium ion transference number, low interfacial resistance, excellent thermal and electrochemical stability, and sufficient mechanical strength.^[4] However, the state-of-the-art polymer SSEs still cannot meet all these desired requirements.

Polyethylene oxide (PEO) is the most commonly used polymer matrix for SSEs. However, PEO-based SSEs suffer from low ionic conductivity at room temperature in the order of 10^{-8} to $10^{-7} \text{ S cm}^{-1}$.^[4] Therefore, extensive studies have focused on introducing inorganic materials into the polymer matrix to enhance the ionic conductivity of polymer electrolytes. Since

H. Chen, D. Adekoya, L. Hencz, Prof. H. Zhao, Prof. S. Zhang
Centre for Clean Environment and Energy
Griffith University
Gold Coast, Queensland 4222, Australia
E-mail: s.zhang@griffith.edu.au

Dr. J. Ma, Prof. G. Cui
Qingdao Industrial Energy Storage Research Institute
Qingdao Institute of Bioenergy and Bioprocess Technology
Chinese Academy of Sciences
Qingdao 266101, China
E-mail: cuigl@qibebt.ac.cn

S. Chen, Prof. C. Yan
School of Chemistry
Physics and Mechanical Engineering
Queensland University of Technology (QUT)
Brisbane, Queensland 64001, Australia

 The ORCID identification number(s) for the author(s) of this article can be found under <https://doi.org/10.1002/aenm.202000049>.

DOI: 10.1002/aenm.202000049

the first report of polymer electrolyte with α - Al_2O_3 , many nano-materials have been applied to polymer electrolytes, such as Fe_2O_3 ,^[8] Al_2O_3 ,^[9,10] TiO_2 ,^[9,10] Y_2O_3 -doped ZrO_2 ,^[11] ZnAl_2O_4 ,^[12] CeO_2 ,^[13] SiO_2 ,^[10] Sm_2O_3 ,^[14] halloysite nanoclay (HNT),^[15] $\text{Mg}_2\text{B}_2\text{O}_5$,^[16] and montmorillonite (LiMNT),^[17] which highlight that inorganic materials are able to improve the electrochemical stability and mechanical strength of ASSBs. Besides these oxides, some other types of composite electrolytes, such as $\text{Li}_7\text{La}_3\text{Zr}_2\text{O}_{12}/\text{PEO}$ and $\text{Li}_{6.75}\text{La}_3\text{Zr}_{1.75}\text{Ta}_{0.25}\text{O}_{12}/\text{Li}_3\text{OCl}$,^[18] have also been widely investigated as they exhibit acceptable ionic conductivity and favorable interfacial contact with electrodes, resulting in enhanced electrochemical performance of ASSBs.^[19] Meanwhile, inorganic materials with oxygen vacancies, which can be positively charged on the surface, have strong interactions with the electrolyte salt anion, thereby releasing more Li^+ ions and subsequently improving ionic conductivity of polymer electrolytes.^[11,20] However, the mechanism behind these effects is still unclear. Understanding of the mechanism may lead to more rational approaches to build high-performance ASSBs.

Owing to the rich oxygen vacancies on its surface, CeO_2 has been used in various applications, including ionic electrolytes,^[21,22] catalysis,^[23] and optical coatings.^[24] The concentration of oxygen vacancies can be further increased through elemental calcium (Ca) doping.^[25] Combining the merits of structural design and surface functionalization, we employed Ca- CeO_2 nanotubes to improve the electrochemical and mechanical properties of PEO-based polymer electrolyte. The Ca- CeO_2 nanotubes can provide continuous ionic conducting pathways and an effective percolation network. Furthermore, the hollow structure in Ca- CeO_2 nanotubes can provide maximum contact area with PEO-based electrolyte.

In this work, we treated Ca- CeO_2 nanotubes at various doping levels via electrospinning and subsequent high-temperature treatment to obtain optimum ionic conductivity. It is demonstrated that the ionic conductivity and transference number of Ca- CeO_2 /lithium bis(trifluoromethanesulfonyl) imide (LiTFSI)/PEO electrolyte can reach $1.3 \times 10^{-4} \text{ S cm}^{-1}$ and 0.453 at 60 °C, respectively. More importantly, various electrochemical, chemical, and mechanical characterizations and computational calculations are conducted to investigate the mechanism of the improved battery performance, especially the interaction between Ca- CeO_2 and LiTFSI. After assembly with LiFePO_4 cathode and lithium anode, the ASSBs deliver an initial discharge of 164 mAh g⁻¹ at 0.1 C, and even 100 mAh g⁻¹ at high current density of 2 C at 60 °C with a wide voltage window

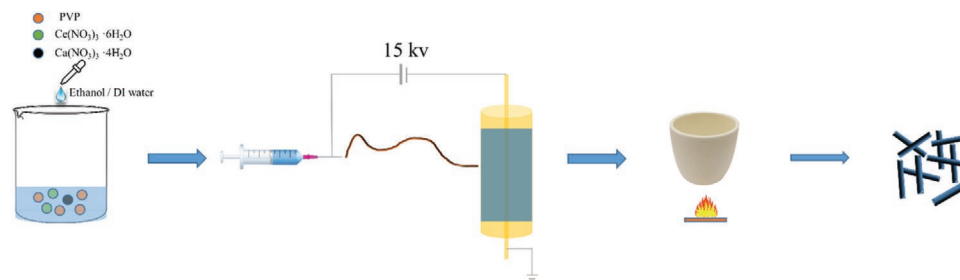
of 2.5–4.1 V. Impressively, the discharge capacity of ASSBs remains at 93 mAh g⁻¹ after 200 cycles at 1 C.

2. Results and Discussion

2.1. Synthesis and Characterization of Ca- CeO_2 Nanotubes

In order to enhance the ionic conductivity of PEO-based electrolyte, inorganic materials are usually introduced, especially oxygen-vacancy-rich materials.^[26] In this work, we used electrospinning to fabricate the Ca- CeO_2 nanotubes to achieve high-performance PEO-based electrolyte. It is well established that the Ca doping is a facile, low-cost and effective method to obtain more oxygen vacancies for CeO_2 .^[21,27] As illustrated in **Scheme 1**, the synthesis process mainly includes the electrospinning of fiber membrane (as shown in Figure S1, Supporting Information) and removal of supporting fiber under high temperature. The viscosity of the solution plays an important role in the morphology formation of materials during electrospinning.^[28] With the proper viscosity, the solvent molecules containing $\text{Ce}(\text{NO}_3)_3 \cdot 6\text{H}_2\text{O}$ and $\text{Ca}(\text{NO}_3)_2 \cdot 4\text{H}_2\text{O}$ are well dispersed on the outer layer of polyvinylpyrrolidone (PVP) clusters. After drying, the electrostatic forces gradually weaken, and the polymers with inorganic fillers in the outer layer become stable. In the subsequent heat treatment, as the temperature slowly increases, the inner PVP pyrolyzes and shrinks and then moves to the outer layer, whereas the outer layer can maintain its integrity. When the temperature rises higher, the solid polymer fiber will form a hollow structure. As the temperature keeps increasing, the PVP gradually decomposes, and the remaining inorganic materials simultaneously become Ca- CeO_2 products. When the PVP is completely removed, the final Ca- CeO_2 nanotubes will be obtained.^[29]

The as-prepared Ca- CeO_2 nanotubes were characterized and displayed in **Figure 1**. After calcination, a single Ca- CeO_2 phase is obtained (Figure 1a), which is consistent with pure CeO_2 phase (JCPDS ICDD #00-034-0394). It suggests that with appropriate doping concentration, no impurity emerges, indicating that Ca enters the CeO_2 crystal without phase change. However, with increasing of doping level, line broadening in peaks of (111) and (200) and intensity weakening in peaks of (222) and (400) occur (Figure S2, Supporting Information). The trend continues as the concentration of Ca increases, which is consistent with previous observations.^[27,30] This change is due to the larger ionic radius of Ca^{2+} (1.12 Å) than Ce^{4+}



Scheme 1. Schematic illustration of the preparation of Ca- CeO_2 nanotubes.

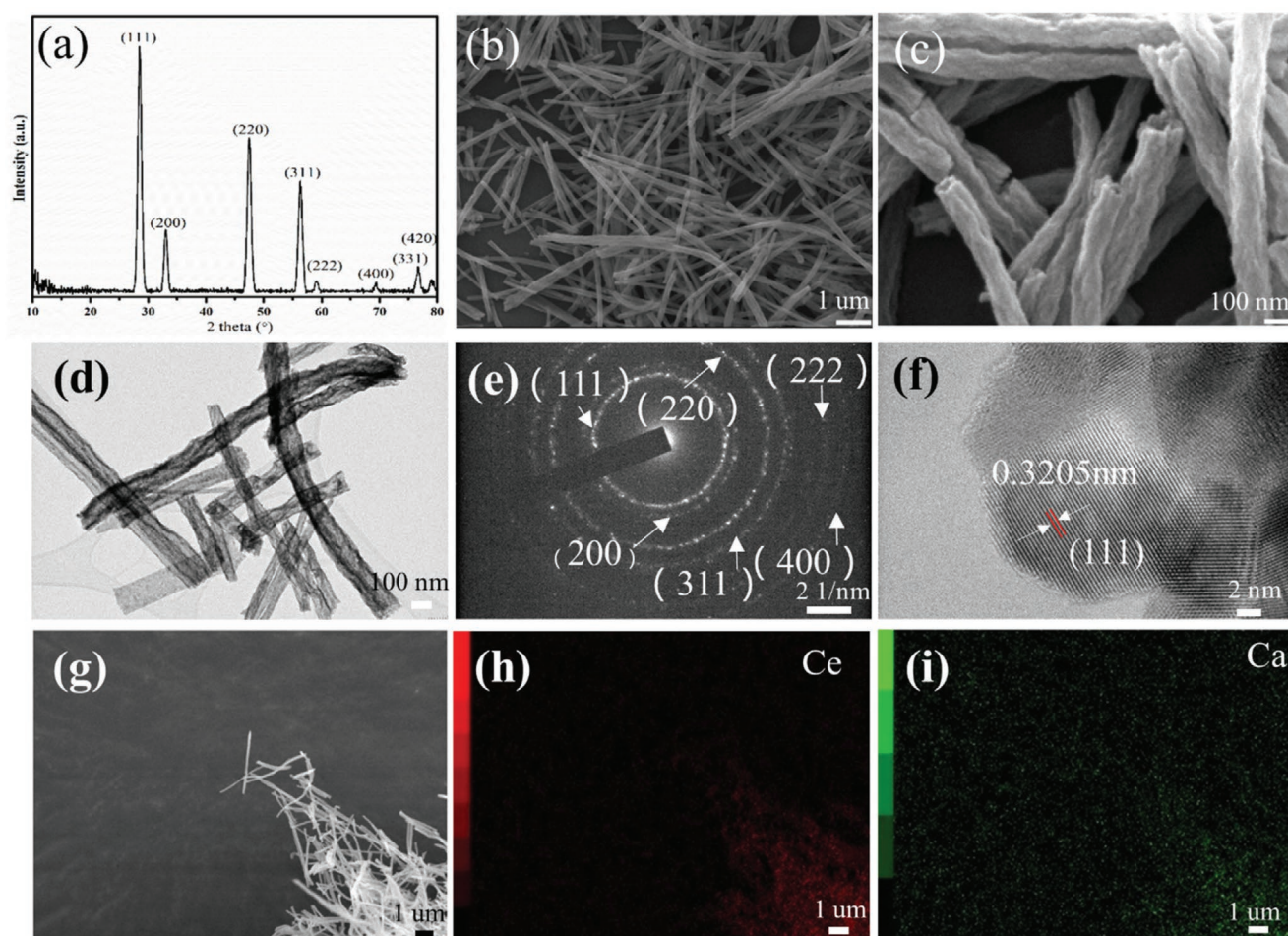


Figure 1. Characterization of Ca-CeO₂ nanotubes (10Ca-CeO₂): a) XRD pattern. b,c,g) SEM images. d) TEM images. e) SAED pattern. f) High-resolution TEM image. h,i) EDS images.

(0.97 Å).^[21] The doping level can also affect the morphology of Ca-CeO₂ nanotubes. With more Ca doping, the surface of Ca-CeO₂ nanotube becomes rougher. Meanwhile, more short nanotubes will generate when the concentration of Ca reaches to 15 mol% (Figure S3, Supporting Information). To gain insight of the nano structure of the as-prepared materials, scanning electron microscopic (SEM) and transmission electron microscopic (TEM) analysis were employed to clearly observe the morphology of Ca-CeO₂. As shown in Figure 1b,c, the Ca-CeO₂ shows a clear nanotube structure with a length range of 1–10 μm and a diameter range of 50–100 nm. The nanotube structure can be further confirmed by TEM image (Figure 1d). The selected area electron diffraction (SAED) image (Figure 1e) and high-resolution TEM image (Figure 1f) reveal a high crystallinity of Ca-CeO₂ nanotubes. The clear lattice fringe with a *d*-spacing of 0.3205 nm correspond to the (111) plane of CeO₂. Compared with the sample 0Ca-CeO₂ in Figure S4 in the Supporting Information, the interplanar spacing increases from 0.3032 to 0.3205 nm after doping because Ca²⁺, with larger ionic radius, replaces Ce⁴⁺.

To investigate the concentration of oxygen vacancies on the Ca-CeO₂ surface before and after Ca doping, X-ray photoelectron spectra (XPS) spectra were obtained to analyze the

valence change. Results reveal that the concentration of Ce³⁺ increases with Ca doping, suggesting that more oxygen vacancies are generated (Figure S5, Supporting Information).^[31] Meanwhile, the Ca doping can also introduce more electrons, leading to a higher electrical conductivity.^[32] Normally, the high electrical conductivity in SSEs will cause lithium dendrite during cycles. Fortunately, the electrical conductivity of Ca-CeO₂ is negligible when Ca-CeO₂ is mixed with insulating PEO polymer.^[20] The Ca distribution in Ca-CeO₂ nanotubes can be further confirmed by the SEM image (Figure 1g) and elemental mapping images (Figure 1h,i), demonstrating that Ca element is uniformly distributed in the nanotubes.

2.2. Preparation and Characterization of Ca-CeO₂/LiTFSI/PEO Composite Electrolyte

The Ca-CeO₂/LiTFSI/PEO composite electrolytes were prepared by solvent-casting method and studied by structural analysis and mechanical tests as depicted in Figure 2. After the removal of the solvent, the rigid-flexible electrolyte films with modified bacterial cellulose were obtained (Figure 2a). The bacterial cellulose makes electrolyte film highly processable and

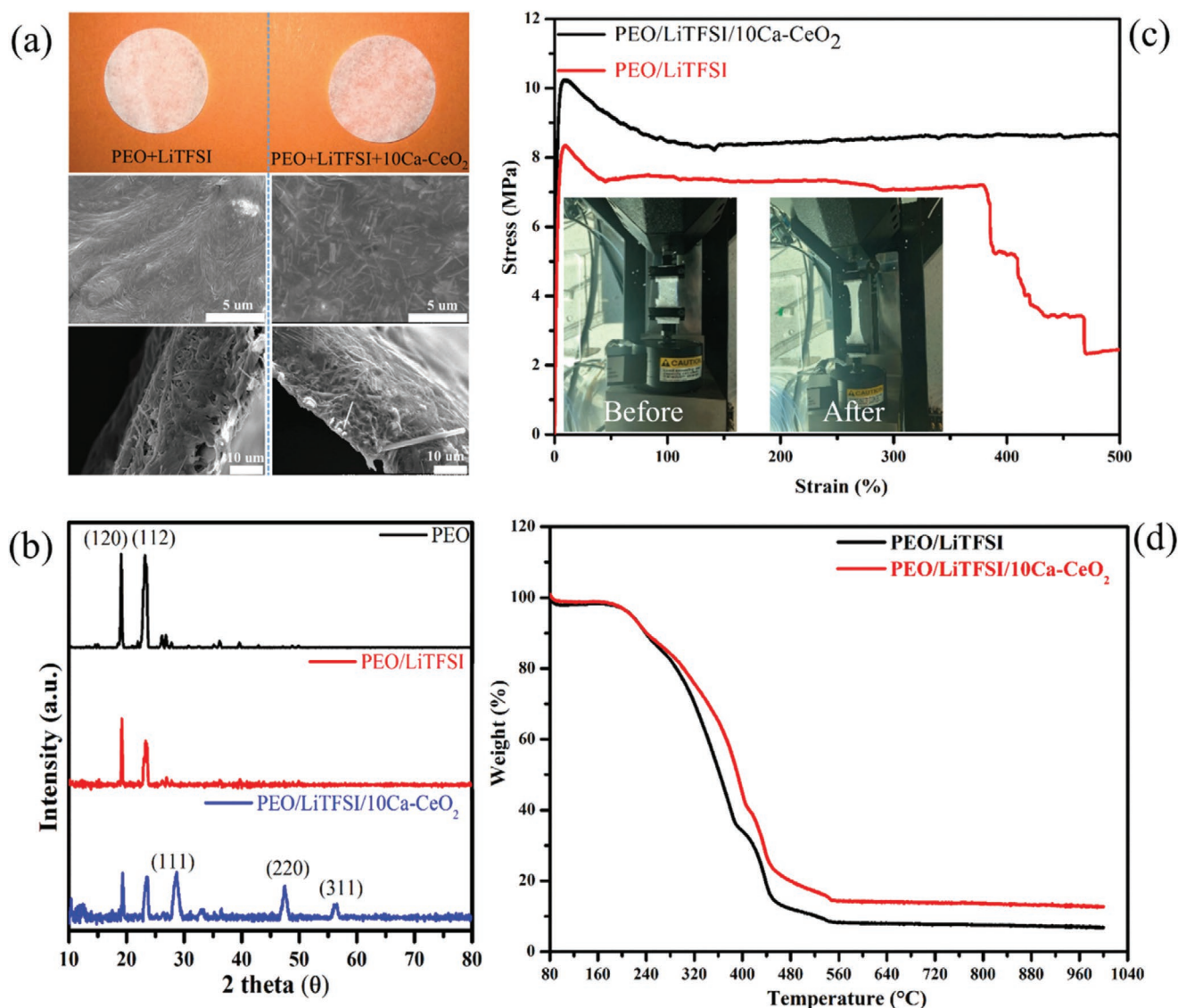


Figure 2. a) Optical images (top) and SEM images (middle and bottom) of PEO/LiTFSI (left) and PEO/LiTFSI/10Ca-CeO₂ (right) electrolyte films. b) XRD patterns of pure PEO, PEO/LiTFSI, and PEO/LiTFSI/10Ca-CeO₂ films. c) Stress-strain curves of PEO/LiTFSI and PEO/LiTFSI/10Ca-CeO₂ films (inset: the photos of PEO/LiTFSI/10Ca-CeO₂ film at initial and tension state). d) TGA curves of PEO/LiTFSI and PEO/LiTFSI/10Ca-CeO₂ films.

greatly enhances the mechanical integrity simultaneously.^[33] Because of the bacterial cellulose as a supporting material, SSEs are easily prepared into thin films with a thickness of around 30 μm. Meanwhile, Ca-CeO₂ nanotubes can be visibly observed in the PEO/LiTFSI/10Ca-CeO₂ electrolyte. To further observe the polymer electrolyte inside of the nanotube, the high-resolution SEM image of PEO/LiTFSI/10Ca-CeO₂ film was obtained. It can be clearly seen that the nanotube of Ca-CeO₂ is filled with polymer electrolyte (Figure S6, Supporting Information). The components in the SSEs were further confirmed by PEO/LiTFSI/10Ca-CeO₂ X-ray diffraction (XRD) patterns in Figure 2b. As LiTFSI is dissolved into the PEO host, no clear diffraction peaks of crystal LiTFSI exist in both electrolytes. Additionally, the peaks of (120) and (112) for PEO weaken after addition of Ca-CeO₂ nanotubes, indicating that the crystallinity degree of PEO is decreased.^[26] The quantitative analyses of the

crystallinity degree were conducted based on XRD patterns. It suggests that with the addition of LiTFSI and Ca-CeO₂, the crystallinity degree of PEO significantly decreases from 69.60% to 47.69% (Figure S7, Supporting Information).

The mechanical strength and flexibility of polymer electrolyte is vital to suppress lithium dendrites and fabricate flexible batteries. Therefore, strain-stress curves are obtained to study the mechanical properties of electrolyte films. As shown in Figure 2c, both samples experience a softening process until the stress reaches the maximum value, which is followed by a quasiplateau region where the films flow with very high plastic strains. However, the crack and stress failure occurs when the strain increases to 370% in PEO/LiTFSI film. In contrast, the film with Ca-CeO₂ can bear a 500% strain state. Meanwhile, the PEO/LiTFSI/10Ca-CeO₂ film has a maximum stress of 10.2 MPa, which is larger than that in PEO/LiTFSI film. The

enhanced mechanical strength is attributed to Ca–CeO₂ nanotubes incorporating into the PEO polymer matrix.^[34] The mechanical strength is further enhanced by introducing modified bacterial cellulose as displayed in Figure S8 in the Supporting Information.

As ASSBs normally work at various temperature ranges, thermal stability is important for SSEs, especially polymeric electrolytes. In Figure 2d, the thermogravimetric analysis (TGA) curves of PEO/LiTFSI and PEO/LiTFSI/10Ca–CeO₂ films can be observed from 80 to 1000 °C. Below 200 °C, the weight loss is about 2% in both samples, which is attributed to the water absorbed from the atmosphere. From 200 to 640 °C, the main weight loss occurs because PEO and LiTFSI decompose. Finally, the remaining mass in PEO/LiTFSI and PEO/LiTFSI/10Ca–CeO₂ films is 8.33% and 13.28%, respectively. The difference of 4.95 % in the remaining mass is due to the thermal stability of Ca–CeO₂ as the final products can only be from LiTFSI decomposition and unreacted Ca–CeO₂. The TGA results demonstrate that Ca–CeO₂ nanotubes can improve the thermal stability of polymer electrolytes to some extent. To test the membrane integrity directly at high temperatures, the PEO/LiTFSI and PEO/LiTFSI/10Ca–CeO₂ films were heated to 120 °C. Results show that the PEO/LiTFSI film starts to melt immediately and becomes viscous liquid completely in 5 min (Figure S9, Supporting Information). However, the PEO/LiTFSI/10Ca–CeO₂ film can maintain its integrity under the same conditions. Additionally, the incorporated Ca–CeO₂ nanotubes can be clearly observed. Thus, the addition of the Ca–CeO₂ will lead to enhanced membrane integrity. Unlike other rechargeable battery systems, SSEs can address safety issues because they are generally fire-retardant compared to batteries using liquid electrolytes. Thus, the combustion test was conducted to compare the flame-retardation of liquid electrolytes and the as-prepared SSEs. As shown in Figure S10 in the Supporting Information, the commercial liquid electrolyte burns instantly and brightly when it gets close to the ignition source and burns rapidly into ashes. However, the PEO/LiTFSI film is easily ignited but without continuous combustion. When the fire is quenched, the PEO/LiTFSI film becomes a sticky liquid. In comparison, the PEO/LiTFSI/10Ca–CeO₂ film can suppress burning significantly and maintain its integrity. Consequently, the incorporation of Ca–CeO₂ nanotubes into the PEO electrolyte can improve flame retardancy, which will provide enhanced safety for LIBs.

2.3. Electrochemical Characterization of Ca–CeO₂/PEO Composite Electrolyte

Electrochemical stability against high voltage and Li metal is a crucial parameter to ASSBs. To evaluate the electrochemical stability of polymer electrolytes against high voltage, linear sweep voltammetry (LSV) was conducted to investigate the electrochemical window using Li/SSE/SS cells at 60 °C. The PEO/LiTFSI/10Ca–CeO₂ electrolyte maintains oxidative stability to over 4.5 V (Figure 3a). In contrast, oxidation occurs at around 4.2 V in the PEO/LiTFSI electrolyte. The high stability of the PEO/LiTFSI/10Ca–CeO₂ film at high voltage enables it to match high-voltage cathode materials. The lithium ion

transference number (t^+) greatly determines the ionic conductivity of the electrolytes. To obtain the t^+ values, chronoamperometry tests were carried out for polymer electrolytes with and without Ca–CeO₂ nanotubes. The obtained chronoamperometry curves and AC impedance spectra are shown in Figure 3b and Figure S11 in the Supporting Information, respectively. Results illustrate that the t^+ value increases from 0.156 to 0.453 by adding Ca–CeO₂ nanotubes. It can also be demonstrated that the PEO/LiTFSI/10Ca–CeO₂ electrolyte has much lower resistance. The electrochemical stability against high voltage, increased t^+ value and reduced resistance are ascribed to the dissociation of LiTFSI ion pairs by Ca–CeO₂ nanotubes which can promote the local relaxation and segmental motion, resulting in more free Li⁺ ions.^[35]

To gain insight into the stability of SSE films against lithium metal, the lithium plating/stripping behavior and cycling stability were examined by galvanostatic discharge/charge voltage profiles in symmetric Li/Li batteries with SSE films. The Li/SSE/Li cells were charged and discharged for 0.5 h under the current densities of 0.02, 0.05, 0.1, and 0.3 mA cm^{−2} at 60 °C. The cell with Ca–CeO₂ nanotubes has lower polarization voltage compared with Li/(PEO/LiTFSI)/Li symmetric cell at all current densities (Figure 3c,d). The Li/(PEO/LiTFSI/10Ca–CeO₂)/Li cell exhibits a stable plating/stripping process even at high rates of 0.3 mA cm^{−2}. On the contrary, drastic amplitude fluctuation occurs in the Li/(PEO/LiTFSI)/Li cell when the current density increases to 0.3 mA cm^{−2}. Figure 3e displays the cycling stability of symmetric cells at a current density of 0.1 mA cm^{−2} for 1000 h. The voltage of plating and stripping of Li in the Li/(PEO/LiTFSI)/Li cell increases greatly with cycling. After cycling for near 700 h, the voltage abruptly drops to 0 V, indicating that battery failure occurs due to Li dendrite growth. In contrast, the symmetric battery with PEO/LiTFSI/10Ca–CeO₂ electrolyte exhibits an excellent flat and stable voltage plateau for 1000 h. An enlarged view of the voltage profiles are also displayed in Figure 3e, showing that the cell has much lower polarization voltage after the addition of Ca–CeO₂ nanotubes. To better understand the lithium plating/stripping behavior, the morphology of Li metal before and after cycles in both polymer electrolytes was observed. The pure Li metal before the cycle has a smooth and uniform morphology (Figure S12a, Supporting Information). After long-term cycles in PEO/LiTFSI, Li dendrites are formed with a much higher surface area (Figure S12b, Supporting Information). In contrast, a relatively smooth and dense morphology is formed in PEO/LiTFSI/10Ca–CeO₂ though small amounts of lithium dendrites on the surface (Figure S12c, Supporting Information). This observation is in agreement with the improved cycling stability in Li/SSE/Li symmetrical cells. The outstanding ability of PEO/LiTFSI/10Ca–CeO₂ electrolyte to suppress lithium dendrite growth is attributed to its high lithium ionic transportation that induces the uniform deposition of lithium metal.^[36] Meanwhile, the increased mechanical strength of polymer electrolyte film can greatly reduce the risk of short-circuiting by lithium dendrites.^[37] The results illustrate that the incorporation of Ca–CeO₂ nanotubes into the PEO-based electrolyte can effectively restrain the lithium dendrite growth.

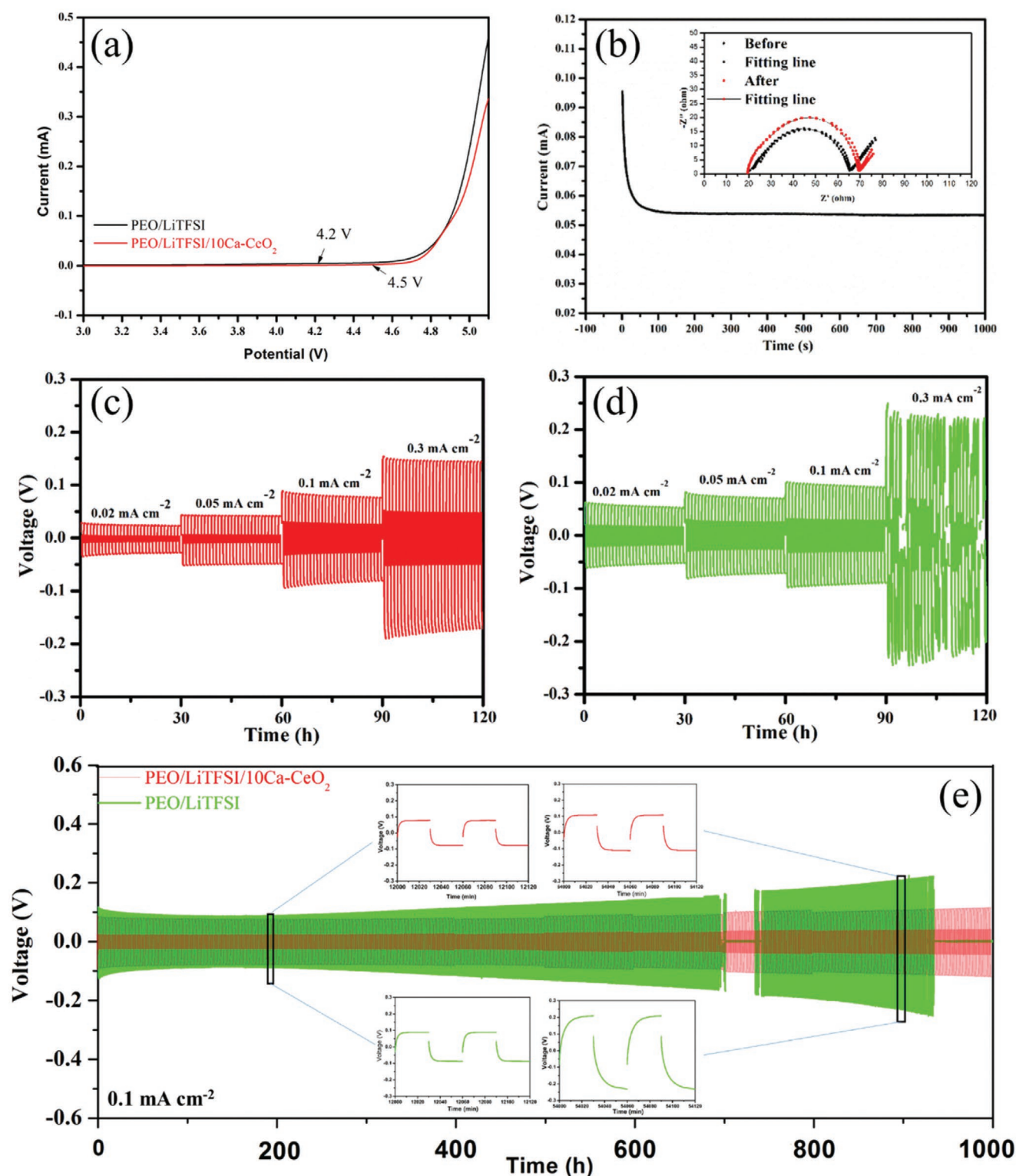


Figure 3. a) LSV curves of PEO/LiTFSI and PEO/LiTFSI/10Ca-CeO₂ films at a scanning rate of 1 mV s⁻¹ at 60 °C. b) The chronoamperometry curves of PEO/LiTFSI/10Ca-CeO₂ film at a potential step of 10 mV at 60 °C. The inset figure shows AC impedance spectra of the same cell before and after polarization. Voltage-time profiles of c) Li/(PEO/LiTFSI/10Ca-CeO₂)/Li and d) Li/(PEO/LiTFSI)/Li cells at 0.02, 0.05, 0.1, and 0.3 mA cm⁻² under 60 °C. e) Voltage-time profiles of Li metal plating/stripping as a function of cycle number at 0.1 mA cm⁻² and 60 °C. The plating Li capacity is 0.05 mAh cm⁻² per cycle.

2.4. Study on the Interaction between Organic and Inorganic Components and Lithium Salts

Based on previous research of inorganic components in polymer electrolytes, the working mechanism of Ca–CeO₂ nanotubes in PEO-based electrolytes has been proposed and can be explained from two aspects.^[15,16,26,38] Firstly, the inorganic Ca–CeO₂ nanotubes will hinder the reorganization of polymer chains and reduce the crystallization degree of the polymer host, thereby increasing the dipole moment of the PEO chains.^[9,39] This explanation can be confirmed by the XRD patterns as shown previously. Secondly, based on the Lewis acid–base interaction, the Ca–CeO₂ nanotubes possess abundant oxygen vacancies, which is well known as an area of positive potential, providing a strong affinity between inorganic nanotubes and TFSI[−] anion groups.^[11,38,40] Furthermore, thanks to their hollow structure and large surface area, the nanotubes provide more active sites between inorganic components and lithium salts in polymer electrolytes. The interaction between Ca–CeO₂ and LiTFSI is illustrated in **Figure 4a**. The positively charged oxygen vacancies on the surface of Ca–CeO₂ nanotubes absorb the TFSI[−] group and then separate the Li⁺ ions from the LiTFSI salts. Consequently, more free Li⁺ ions will interact with the EO units on the PEO polymer and be transported with the segmental motion of PEO chains. Meanwhile, the nanotubes will form continuous 3D pathways for Li⁺ transport. Therefore, the lower crystallization degree of PEO polymer, more free Li⁺ ions, and fast Li⁺ transport pathways caused by the addition of Ca–CeO₂ nanotubes work comprehensively to achieve excellent high-performance ASSBs.

To verify the proposed hypothesis, Fourier transform infrared (FTIR) characterizations were conducted to investigate the interaction between Ca–CeO₂ nanotube and LiTFSI salt as well as the effects of the doping level. **Figure 4b** shows the complete FTIR spectra of PEO/LiTFSI/Ca–CeO₂ electrolyte with various doping levels and Ca–CeO₂-free electrolyte from 4000 to 400 cm^{−1}. As it is difficult to capture the tiny distinction in full-range spectra, the detailed spectra in the range of 1400–1150 cm^{−1} are presented in **Figure 4c**. Combined with the FTIR spectra of pure components in **Figure S13** in the Supporting Information, it can be seen that the peaks at near 1351, 1341, 1281, and 1241 cm^{−1} belong to PEO. The other main peaks correspond to the asymmetric and symmetric stretching of –SO₂ and –CF₃ structures in LiTFSI.^[15,16] When LiTFSI is dissolved into PEO host, the shifting and splitting of peaks at around 1325, 1244, and 1199 cm^{−1} occurs, illustrating the dissociation of LiTFSI in PEO polymer.^[15,16,41] Subsequently, when 10Ca–CeO₂ nanotubes are added to PEO/LiTFSI electrolyte, the peaks at 1332.2 and 1303.2 cm^{−1}, corresponding to –SO₂ stretching, shift to 1332.9 and 1299.3 cm^{−1}, respectively. Meanwhile, similar shifts of peaks at 1251.7 and 1228.7 cm^{−1} to 1251.2 and 1229.6 cm^{−1} for symmetric stretching of –CF₃ and 1198.1 and 1183.2 cm^{−1} to 1193.2 and 1180 cm^{−1} for asymmetric stretching of –CF₃ can also be observed, respectively. The shift degree reaches the maximum value when the dopant is 10 % mol. These shifts in –SO₂ and –CF₃ groups suggest the strong interaction between Ca–CeO₂ nanotubes and LiTFSI.^[15,16,41]

When TFSI[−] groups interact with Ca–CeO₂ nanotubes, more free Li⁺ ions will be released, resulting in enhanced ionic

conductivity for polymer electrolyte. To further confirm our assumption, the Arrhenius plots of PEO/LiTFSI and PEO/LiTFSI/Ca–CeO₂ electrolytes are obtained and shown in **Figure 4d**. The Arrhenius plots are derived from the impedance spectra as a function of temperature. As shown in **Figure 4e**, the impedance of PEO/LiTFSI/10Ca–CeO₂ electrolyte decreases dramatically when temperature increases. When the doping level goes up to 10 mol%, the electrolyte achieves the highest ionic conductivity (1.3×10^{-4} S cm^{−1} at 60 °C). The excess dopants in Ca–CeO₂ nanotubes may affect the crystal structure and morphology as shown in **Figures S2 and S3** in the Supporting Information, thereby leading to a decrease of ionic conductivity.^[27,42] Therefore, the enhanced ionic conductivity of PEO-based electrolytes can be ascribed to the interaction of Ca–CeO₂ nanotubes with LiTFSI, resulting in more free Li⁺ ions to travel along the PEO chains.

The –SO₂ and –CF₃ groups are the interaction sites in LiTFSI. However, the ways these sites interact with Ca–CeO₂ are difficult to detect. To better understand the interaction sites between LiTFSI and CeO₂ nanotubes, an atomic scale density functional theory (DFT) calculation was conducted. Firstly, the most stable molecular structures of the LiTFSI and CeO₂ with (111) surface are built as shown in **Figure S14** in the Supporting Information. Similar to previous results, a preliminary study of the structure of CeO₂ (111) surface shows that the O terminated surface is the energetically stable adsorption surface.^[43] The significance of this atomic-scale calculation from first principle is in line with the fundamental principle of SSEs systems in that, the TFSI[−] anion should be effectively immobilized on the surface of the substrate material so that cationic Li⁺ ions can freely transport through the PEO/LiTFSI matrix near the Ca–CeO₂.^[44] To study this, the binding energy of Li⁺ with TFSI[−] in LiTFSI and in the CeO₂+LiTFSI with and without oxygen vacancy were calculated and shown in **Figure 5a,b** and **Figure S15** in the Supporting Information. The –SO₂ group in TFSI[−] interacts with Ce atoms on the CeO₂ surface, and the binding energy of Li⁺ to TFSI[−] decreases from about 5.78 to 5.68 eV when one oxygen vacancy exists, indicating a lesser hindrance to Li⁺ freedom. More significantly, when Ca is doped and LiTFSI is immobilized on the surface of CeO₂, a –O^{2−}–Ca²⁺–F bond is formed and the Li binding energy is determined to be 4.52 eV, indicating a decrease in the binding energy of TFSI[−] to Li by about 1.16 eV (**Figure 5c,d**). This lower binding energy of TFSI[−] to Li⁺ means that LiTFSI is easily dissociated and Li⁺ can be rapidly transported through the material.^[44] These results also confirm the interaction between –CF₃ groups in TFSI[−] and Ca–CeO₂. It also should be noted that the Ca doping could provide stronger dissociation ability than oxygen vacancies. However, much more oxygen vacancies exist on the surface of Ca–CeO₂ than that created by Ca-doping. In practice, the enhanced dissociation of LiTFSI salt is attributed to synergistic effects by both oxygen vacancy and Ca-doping, which is also confirmed by FTIR spectra (**Figure 4c**). Thus, the interaction of Ca–CeO₂ with the anion portion (TFSI[−]) of the lithium salt, namely strong chemical coupling between Ca–CeO₂ and TFSI[−] anions through –SO₂–Ce–O– and –O–Ca–CF₃– bonding, results in decreased binding force between TFSI[−] and Li⁺, thereby promoting dissociation of lithium salts to release more Li⁺ and subsequently fostering rapid Li⁺ migration and improved ionic conductivity.^[11,15]

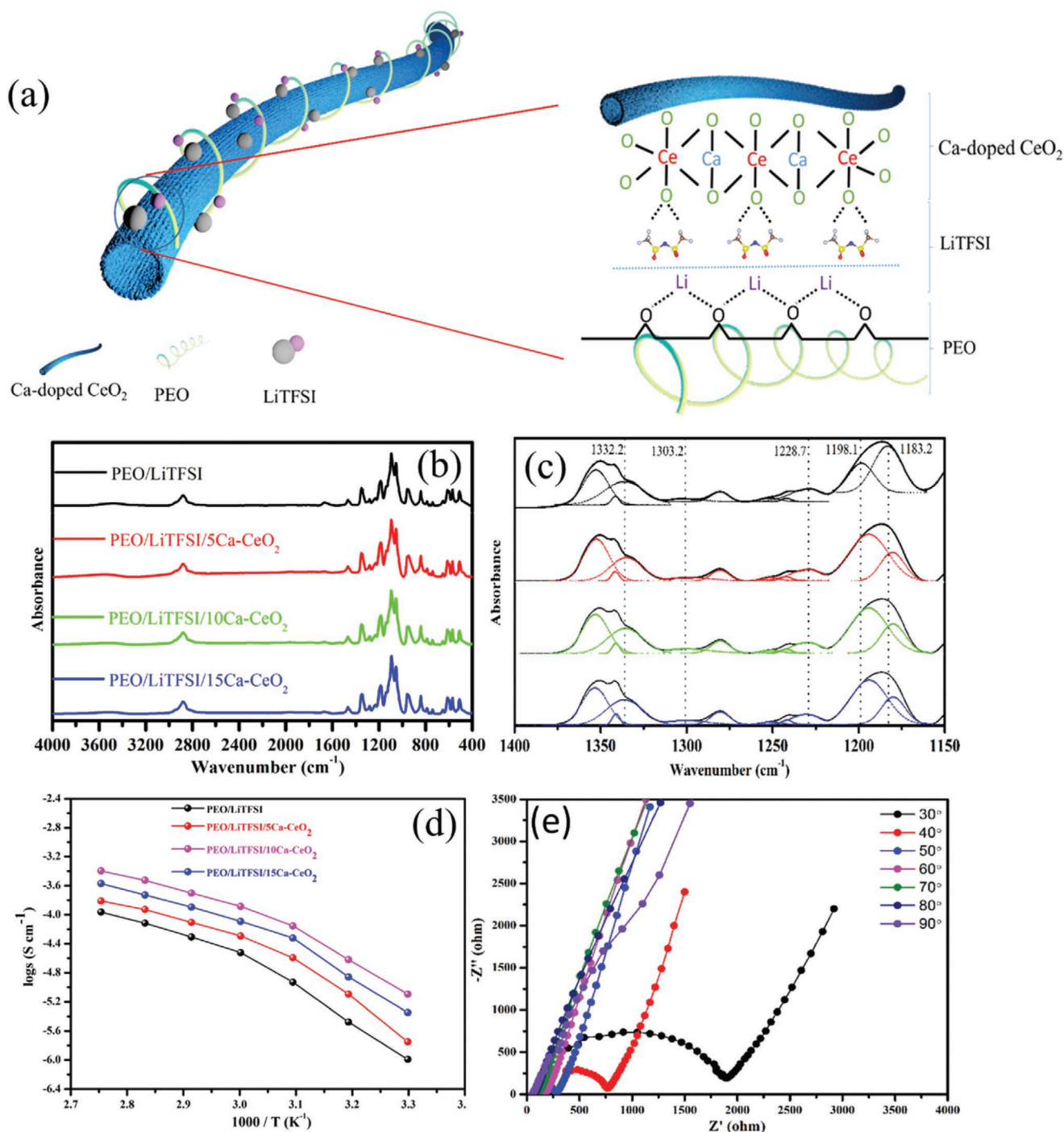


Figure 4. a) Schematic illustration of mechanism for enhanced Li ion transport in PEO-based electrolyte by Ca-CeO₂ nanotubes. FTIR spectra for PEO/LiTFSI electrolyte and PEO/LiTFSI/Ca-CeO₂ electrolyte with various Ca doping levels at b) 4000–400 cm⁻¹ and c) 1400–1150 cm⁻¹. d) Arrhenius plots of PEO/LiTFSI and PEO/LiTFSI/Ca-CeO₂ electrolytes. e) Impedance spectra of SS/(PEO/LiTFSI/10Ca-CeO₂)/SS cell from 30 to 90 °C.

2.5. Battery Performance of Ca-CeO₂/PEO Composite Electrolyte

To evaluate the galvanostatic performance of the polymer electrolyte, ASSBs were assembled and tested at 60 °C. **Figure 6a** presents the rate performance of LiFePO₄ cathode with PEO/LiTFSI and PEO/LiTFSI/10Ca-CeO₂ electrolyte. The battery

with PEO/LiTFSI/10Ca-CeO₂ electrolyte delivers higher capacity than that with PEO/LiTFSI, especially at high current densities, indicating that the addition of Ca-CeO₂ nanotubes can greatly increase rate capability. Specifically, the battery with Ca-CeO₂ shows high initial capacities of about 164, 159, 147, 121, and 100 mAh g⁻¹ at 0.1, 0.2, 0.5, 1, and 2 C, respectively. The related charge-discharge curves in Figure S16 in the Supporting

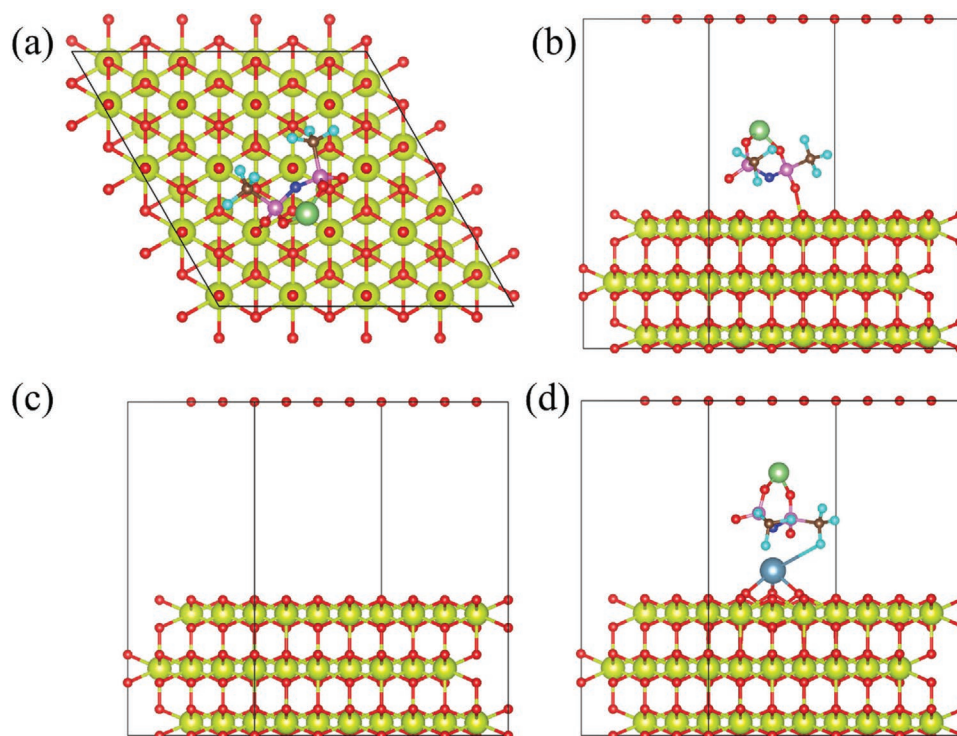


Figure 5. a) Top and b) side view of the crystallographic structure of LiTFSI adsorbed on the surface of the O-terminated CeO_2 (111) surface with oxygen vacancy. Ce-terminated CeO_2 (111) surface was first considered as a stable substrate to adsorb LiTFSI; however, it decomposed TFSI^- and then became O terminated. Therefore, O-terminated CeO_2 (111) was chosen as a stable and preferred substrate for the lithium salt. c) Side view of the lowest energy configuration for CeO_2 (111) surface atomic structure. d) The crystallographic structure of LiTFSI adsorbed on the O-terminated (111) surface of the Ca- CeO_2 nanotube with one oxygen vacancy, O in red, Ca in greenish blue, F in cyan, C in brown, N in deep blue, S in Magenta and Li in green, Ce atoms in light reflective yellow.

Information further confirm the stable charge–discharge process at all rates. Moreover, the PEO/LiTFSI/10Ca- CeO_2 -based battery has flatter working platforms and shows a lower polarization than the PEO/LiTFSI-based battery (Figure 6b). This phenomenon is ascribed to the higher ionic conductivity of SSE after incorporating Ca- CeO_2 nanotubes into the PEO host, resulting in small resistance during charging and discharging. It should also be noted that the first charge capacity of the PEO/LiTFSI/10Ca- CeO_2 -based battery is beyond its theoretical capacity of 170 mAh g^{-1} , which may be attributed to the wetting process between the electrolyte and electrodes.^[45]

The higher rate capability and lower polarization after the addition of Ca- CeO_2 nanotubes can also be explained by CV curves as shown in Figure S17 in the Supporting Information. An oxidation peak at about 3.6 V and one reduction peak at about 3.2 V can be clearly observed in both samples, corresponding to deintercalation and intercalation of Li ions. The smaller voltage difference between oxidation and reduction peaks in the PEO/LiTFSI/10Ca- CeO_2 -based battery reflects fast electrochemical kinetics and high electrochemical reversibility.^[45] Meanwhile, the high overlapping degree of CV curves during the first three cycles in the PEO/LiTFSI/10Ca- CeO_2 -based battery reveals better cycling stability compared to the PEO/LiTFSI-based battery. Subsequently, the long-term cycling of ASSBs was investigated. It is remarkable that the discharge capacity of LiFePO_4 battery with PEO/LiTFSI/10Ca- CeO_2 electrolyte remains 93 mAh g^{-1} after 200 cycles at 1 C (Figure 6c)

and 157 mAh g^{-1} after 40 cycles at 0.2 C (Figure 6d). On the contrary, the PEO/LiTFSI-based battery shows poor cycle stability with capacity retention of 79% after 40 cycles at 0.2 C and 35% after 200 cycles at 1C. The cycle stability of ASSBs is ascribed to the high ionic conductivity of polymer electrolyte and sufficient mechanical strength to suppress Li dendrites during long-term cycling.

PEO-based electrolyte is considered low-voltage SSE as it will be oxidized at a voltage over 3.9 V.^[46] Fortunately, the addition of Ca- CeO_2 nanotubes can widen the electrochemical window of PEO-based electrolyte. Herein, a LiCoO_2 cathode is chosen to investigate the compatibility of PEO-based electrolytes with high-voltage cathodes. As shown in Figure 6e and Figure S18 in the Supporting Information, the LiCoO_2 cathode with PEO/LiTFSI/10Ca- CeO_2 electrolyte was cycled between 2.5 and 4.3 V at 0.1 C and 60 °C. The characteristic plateau of the LiCoO_2 cathode can be observed in the initial five cycles, and a high specific capacity of 113 mAh g^{-1} has been achieved in the third cycle (Figure 6e). The smooth charge and discharge curves indicate that the PEO/LiTFSI/Ca- CeO_2 electrolyte can work steadily at a high voltage of up to 4.3 V. In contrast, the $\text{Li}/(\text{PEO}/\text{LiTFSI})/\text{LiCoO}_2$ battery delivers limited discharge specific capacities of below 50 mAh g^{-1} at 0.1 C. Meanwhile, a clear polarization voltage can be observed in the first charge process. The limited capacity and polarization voltage is mainly ascribed to the relatively low ionic conductivity of PEO/LiTFSI electrolyte. The related cycling performance of

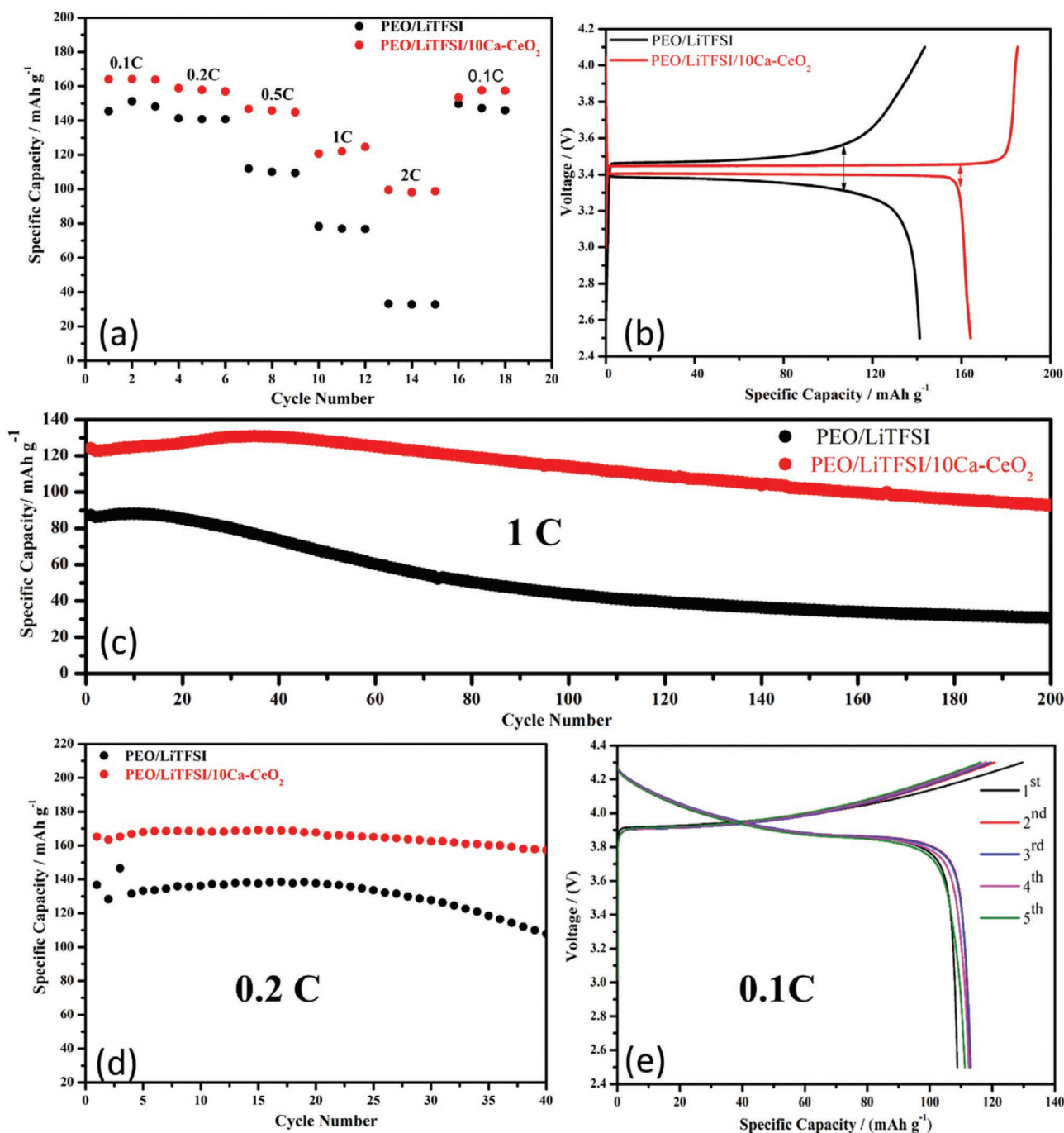


Figure 6. a) Rate performance of PEO/LiTFSI and PEO/LiTFSI/10Ca-CeO₂ electrolyte with LiFePO₄ cathode. b) Charge-discharge curves of the first cycle for all-solid-state LiFePO₄ batteries at 0.1 C. c) Cycle performance of LiFePO₄ batteries at 1 C. d) Cycle performance of LiFePO₄ batteries at 0.2 C. e) Charge-discharge curves of the first five cycles for all-solid-state LiCoO₂ batteries with PEO/LiTFSI/10Ca-CeO₂ electrolyte. All batteries were tested at 60 °C.

the Li/(PEO/LiTFSI/Ca-CeO₂)/LiCoO₂ cell was tested and displayed in Figure S19 in the Supporting Information. It suggests that the addition of Ca-CeO₂ nanotubes significantly improves the high-voltage stability. Therefore, the electrochemical performance of ASSBs indicates that the incorporation of Ca-CeO₂ nanotubes can effectively address two critical challenges, namely low ionic conductivity and poor high-voltage stability, in PEO-based polymer electrolyte.

3. Conclusion

Ca-CeO₂ nanotubes with abundant oxygen vacancies were successfully synthesized via electrospinning and heat treatment. When these Ca-CeO₂ nanotubes and LiTFSI are incorporated into PEO-based electrolyte, the resultant Ca-CeO₂/LiTFSI/PEO composite electrolyte exhibited enhanced ionic conductivity and a wider electrochemical window than the LiTFSI/PEO

electrolyte. A systematic study demonstrated that the improved electrochemical and mechanical performance of PEO-based electrolyte could be attributed to the interactions between LiTFSI and Ca–CeO₂ nanotubes. With excellent mechanical and electrochemical properties, the all-solid-state LiFePO₄ batteries with Ca–CeO₂/LiTFSI/PEO electrolyte exhibited stable cycling performance with high specific capacities. It was also demonstrated that the Ca–CeO₂/LiTFSI/PEO electrolyte could work properly with high-voltage LiCoO₂ cathodes. The working mechanisms were verified by various characterizations and computational calculations. This work suggests that the design of functional inorganic/polymeric composite electrolyte presents a promising strategy to resolve the stubborn barriers (i.e., insufficient contact at the interfaces and ionic conductivity) of ASSBs.

4. Experimental Section

Preparation of Ca–CeO₂ Nanotube: Firstly, 1 mmol Ce(NO₃)₃·6H₂O (>99%, Aldrich) and Ca(NO₃)₂·4H₂O (>99%, Chem-supply) with various molar ratios were dissolved in 4 mL deionized water, and then 2 g PVP (*M_w* = 1 300 000, Aldrich) as polymer host was dissolved in a 8 mL mixture solution of dehydrated alcohol/deionized water (3:1 in volume). Subsequently, the salt solution was dropped slowly into the PVP solution under vigorous stirring. Finally, a transparent gel was obtained after stirring for 3 h. For the electrospinning procedure, the obtained gel was loaded into a 10 mL syringe with a stainless steel (SS) 18G needle. A voltage of 15 kV was applied, and the polymer fiber was collected on a rotating stainless steel drum collector with an aluminum foil coating layer. The collected fiber film was dried at 60 °C under vacuum for 12 h, and then calcined at 600 °C for 6 h in air at a heating rate of 2 °C min^{−1}. To investigate the effects of doping levels, Ca–CeO₂ nanotubes with various concentrations of calcium (0, 5, 10, and 15 mol%) were synthesized and represented as 0Ca–CeO₂, 5Ca–CeO₂, 10Ca–CeO₂, and 15Ca–CeO₂, respectively.

Preparation of SSE Film: The as-obtained Ca–CeO₂ nanotubes, LiTFSI (99.5%, Aldrich) and PEO (*M_w* = 4 × 10⁵, Aldrich) were added to the anhydrous acetonitrile, and mechanically stirred for 24 h to form a homogeneous solution. The weight ratio of PEO, Ca–CeO₂ and LiTFSI was 70:5:25. The solution was cast with a doctor blade on a polytetrafluoroethylene (PTFE) plate and dried in a high-vacuum oven at 60 °C for at least 48 h. For battery testing, the electrolyte film was coated on modified bacterial cellulose to make a rigid-flexible structure with thickness of 30 μm as reported previously.^[33,47] Finally, the electrolyte membrane was stored in an argon-filled glove box.

Preparation of All-Solid-State LiFePO₄/SSE/Li Batteries: The ASSBs were assembled in 2032-type coin cells by contacting a lithium metal anode, the as-prepared Ca–CeO₂/PEO SSE and a LiFePO₄ or LiCoO₂ cathode. The cathode was composed of 80 wt% LiFePO₄ or LiCoO₂, 10 wt% carbon black, and 10 wt% PEO-LiTFSI binder. The cathode composite was added into anhydrous acetonitrile and then coated on aluminum substrate. Subsequently, the acetonitrile solvent was removed at 60 °C under vacuum, and the electrode was punched with a diameter of 11 mm. The batteries were sealed in an argon-filled glove box and then housed at 60 °C for 24 h to reduce the interfacial impedance between electrode and electrolyte.

Material Characterization: XRD analysis (Shimadzu XRD-6000) was used to investigate the crystalline structure of Ca–CeO₂ nanotubes and SSE films by scanning the angular range 10° ≤ 2θ ≤ 80° using Cu Kα radiation (λ = 1.5418 Å). The morphology of Ca–CeO₂ nanotubes and SSE films was revealed by SEM (Hitachi S7100) and TEM (Philips F20). Elemental mapping was conducted on an energy-dispersive X-ray spectroscopy (EDS). The XPS were performed on Kratos Axis ULTRA system. FTIR spectra were obtained on Bruker Vector-22 FTIR

spectrometer in the range of 4000–400 cm^{−1}. TGA and differential scanning calorimetry (DSC) were carried out on a NETZSCHSTA-449 TG analyzer in air in the temperature range of 80–1000 °C at a heating rate of 5 °C min^{−1}. The mechanical stability of SSE films was performed on a microforce tester (MTS Tytron) with a fixed stretching speed of 0.1 mm s^{−1}. The free-standing SSE films were tailored into long strips (2 × 5 cm) with a thickness of 120 μm, and the SSE films with modified bacterial cellulose were 2 × 5 cm with a thickness of 30 μm. Flammability tests of liquid electrolyte (1 M LiPF₆ in ethylene carbonate (EC)/ethyl-methyl carbonate (EMC)) and SSE films were conducted by using a burning torch heater.

Electrochemical Measurements: The lithium transference number (*t⁺*) for the SSE films was measured by chronoamperometry and AC impedance spectra using two lithium metal foils as the nonblocking electrodes. 10 mV was the potential applied across the cells, and electrochemical impedance spectroscopy (EIS) spectra of the cell before and after polarization were obtained from 0.01 to 10⁶ Hz. The *t⁺* values for SSE films were measured and calculated according to the equation^[48]

$$t^+ = \frac{I_{SS}(\Delta V - I_0 R_0)}{I_0(\Delta V - I_{SS} R_{SS})} \quad (1)$$

where *I₀* and *I_{SS}* are the initial and steady-state currents, Δ*V* is the polarization potential at 10 mV, and *R₀* and *R_{SS}* are the initial and steady-state resistance. The ionic conductivities of SSE films were evaluated by the EIS with the frequency range of 0.01–10⁶ Hz between 30 and 90 °C. The SSE films were sandwiched by two SS disks. The equation for calculating the ionic conductivity is

$$\delta = \frac{l}{SR_b} \quad (2)$$

where *l* is the thickness of the electrolyte, *R_b* is the bulk resistance of the electrolyte and the intercept of the x-axis of the straight line, and *S* is the area of the blocking stainless steel electrodes. LSV was tested on Li/SSE/SS cells from 3.0 to 5.1 V. The stripping/plating behavior of SSE films was measured using Li/SSE/Li symmetric cells at a current density of 0.02, 0.05, 0.1, and 0.3 mA cm^{−2}. The long-term stripping/plating performance was tested at 0.1 mA cm^{−2} for 1000 h.

For cell performance with LiFePO₄ cathode, the rate capability of SSBs was measured at 0.1, 0.2, 0.5, 1, and 2 C (1 C = 150 mA g^{−1}). The cycling test was conducted at 0.2 C for 40 cycles and 1 C for 200 cycles. All the batteries were tested between 2.5 and 4.1 V at 60 °C. For the LiCoO₂ cathode, the batteries were cycled at 0.1 C (1 C = 175 mA g^{−1}) between 2.5 and 4.3 V at 60 °C. All the electrochemical tests were carried out using a BioLogic VSP-300 electrochemical workstation and Neware multichannel battery station.

DFT Computation: The DFT calculations were performed with the Vienna ab initio simulation package (VASP) and the Hubbard *U* term (DFT+*U*) method to accurately correct the strong on-site Coulomb interactions of Ca 2s and Ce 4f states. Based on a previous study, the chosen *U* value is 5 eV for Ce.^[49] The supercell model was built from the cubic CeO₂ cell with a lattice constant of *a* = 5.488 Å. For the surface model, the (111) surface was modeled to characterize the surface interactions. The slab model was a *p* (3 × 3) lateral cell with nine atomic layers thickness and a 20 Å vacuum gap in the direction perpendicular to the surface. One Ce atom of the outermost Ce layer (111) slab was replaced by a Ca atom, giving an overall dopant concentration of 3.7%. The bottom four atomic layers were fixed at their bulk-truncated positions, while the top five atomic layers were fully relaxed. Relaxation of the model was carried out until the maximum Hellmann–Feynman force was below 0.01 eV Å^{−1} for the forces and an energy cut-off of 500 eV.

The binding energies of Li in LiTFSI and in the built models were calculated as

$$E_{\text{ads}}(\text{Li on TFSI}) = E(\text{TFSI}) + E(\text{Li}_{\text{atom}}) - E(\text{LiTFSI}) \quad (3)$$

$$E_{\text{ads}}(\text{surface without Ca}) = E(\text{surface} + \text{TFSI}) + E(\text{Li}_{\text{atom}}) - E(\text{surface} + \text{LiTFSI}) \quad (4)$$

$$E_{\text{ads}}(\text{surface with Ca}) = E(\text{surface} + \text{Ca} + \text{TFSI}) + E(\text{Li}_{\text{atom}}) - E(\text{surface} + \text{Ca} + \text{LiTFSI}) \quad (5)$$

where E (surface + LiTFSI) and E (surface) are total energies of the Ca–CeO₂ (111) surface with and without LiTFSI, respectively. E (surface + TFSI) are total energies of the CeO₂ (111) surface with TFSI. E (Li_{atom}) is the energy of bulk lithium metal often used as the reference energy of Li atom.

Supporting Information

Supporting Information is available from the Wiley Online Library or from the author.

Acknowledgements

This work was financially supported by the Australian Research Council (ARC) Future Fellowship and Discovery Project and Griffith University Ph.D. Scholarships. The authors thank the Australian Research Council for support of this project through the LIEF program. DFT resources were provided by the NCI National Facility systems at the Australian National University and the PAWSEY Supercomputing Centre.

Conflict of Interest

The authors declare no conflict of interest.

Keywords

all-solid-state batteries, CeO₂ nanotubes, lithium ion batteries

Received: January 6, 2020

Revised: March 15, 2020

Published online:

- [1] J. Janek, W. G. Zeier, *Nat. Energy* **2016**, 1, 16141.
- [2] a) S. Xia, X. Wu, Z. Zhang, Y. Cui, W. Liu, *Chem* **2019**, 5, 753; b) H. Xiang, J. Chen, Z. Li, H. Wang, *J. Power Sources* **2011**, 196, 8651.
- [3] a) A. Manthiram, X. Yu, S. Wang, *Nat. Rev. Mater.* **2017**, 2, 16103; b) X. Chen, W. He, L.-X. Ding, S. Wang, H. Wang, *Energy Environ. Sci.* **2019**, 12, 938; c) Z. Jiang, H. Xie, S. Wang, X. Song, X. Yao, H. Wang, *Adv. Energy Mater.* **2018**, 8, 1801433.
- [4] D. Zhou, D. Shanmukaraj, A. Tkacheva, M. Armand, G. X. Wang, *Chem* **2019**, 5, 2326.
- [5] L. Xu, S. Tang, Y. Cheng, K. Wang, J. Liang, C. Liu, Y.-C. Cao, F. Wei, L. Mai, *Joule* **2018**, 2, 1991.
- [6] T. Famprikis, P. Canepa, J. A. Dawson, M. S. Islam, C. Masquelier, *Nat. Mater.* **2019**, 18, 1278.
- [7] K. S. Ngai, S. Ramesh, K. Ramesh, J. C. Juan, *Ionics* **2016**, 22, 1259.
- [8] N. S. T. Do, D. M. Schaetzl, B. Dey, A. C. Seabaugh, S. K. Fullerton-Shirey, *J. Phys. Chem. C* **2012**, 116, 21216.
- [9] F. Croce, G. B. Appetecchi, L. Persi, B. Scrosati, *Nature* **1998**, 394, 456.
- [10] J. Zhou, P. S. Fedkiw, *Solid State Ionics* **2004**, 166, 275.
- [11] W. Liu, D. Lin, J. Sun, G. Zhou, Y. Cui, *ACS Nano* **2016**, 10, 11407.
- [12] L. Wang, W. Yang, J. Wang, D. G. Evans, *Solid State Ionics* **2009**, 180, 392.
- [13] A. Dey, S. Karan, S. K. De, *J. Phys. Chem. Solids* **2010**, 71, 329.
- [14] P. P. Chu, M. Jaipal Reddy, *J. Power Sources* **2003**, 115, 288.
- [15] Y. Lin, X. Wang, J. Liu, J. D. Miller, *Nano Energy* **2017**, 31, 478.
- [16] O. Sheng, C. Jin, J. Luo, H. Yuan, H. Huang, Y. Gan, J. Zhang, Y. Xia, C. Liang, W. Zhang, *Nano Lett.* **2018**, 18, 3104.
- [17] L. Chen, W. Li, L.-Z. Fan, C.-W. Nan, Q. Zhang, *Adv. Funct. Mater.* **2019**, 29, 1901047.
- [18] a) Z. Wan, D. Lei, W. Yang, C. Liu, K. Shi, X. Hao, L. Shen, W. Lv, B. Li, Q.-H. Yang, F. Kang, Y.-B. He, *Adv. Funct. Mater.* **2019**, 29, 1805301; b) Y. Tian, F. Ding, H. Zhong, C. Liu, Y.-B. He, J. Liu, X. Liu, Q. Xu, *Energy Storage Mater.* **2018**, 14, 49.
- [19] S. Li, S.-Q. Zhang, L. Shen, Q. Liu, J.-B. Ma, W. Lv, Y.-B. He, Q.-H. Yang, *Adv. Sci.* **2020**, 7, 1903088.
- [20] N. Wu, P. H. Chien, Y. Qian, Y. Li, H. Xu, N. S. Grundish, B. Xu, H. Jin, Y. Y. Hu, G. Yu, J. B. Goodenough, *Angew. Chem., Int. Ed.* **2020**, 59, 4131.
- [21] V. Thangadurai, P. Kopp, *J. Power Sources* **2007**, 168, 178.
- [22] M. Yan, T. Mori, J. Zou, J. Drennan, *J. Am. Ceram. Soc.* **2009**, 92, 2745.
- [23] A. S. Deshpande, N. Pinna, P. Beato, M. Antonietti, M. Niederberger, *Chem. Mater.* **2004**, 16, 2599.
- [24] a) V. Petrovsky, B. P. Gorman, H. U. Anderson, T. Petrovsky, *J. Appl. Phys.* **2001**, 90, 2517; b) M. Yamashita, K. Kameyama, S. Yabe, S. Yoshida, Y. Fujishiro, T. Kawai, T. Sato, *J. Mater. Sci.* **2002**, 37, 683.
- [25] a) X. Chen, G. Li, Y. Su, X. Qiu, L. Li, Z. Zou, *Nanotechnology* **2009**, 20, 115606; b) R. Blumenthal, B. Pinz, *J. Appl. Phys.* **1967**, 38, 2376.
- [26] W. Liu, N. Liu, J. Sun, P.-C. Hsu, Y. Li, H.-W. Lee, Y. Cui, *Nano Lett.* **2015**, 15, 2740.
- [27] L. Truffault, M.-T. Ta, T. Devers, K. Konstantinov, V. Harel, C. Simmonard, C. Andreazza, I. P. Nevirkovets, A. Pineau, O. Veron, J.-P. Blondeau, *Mater. Res. Bull.* **2010**, 45, 527.
- [28] G.-H. An, S.-Y. Jeong, T.-Y. Seong, H.-J. Ahn, *Mater. Lett.* **2011**, 65, 2377.
- [29] C. Niu, J. Meng, X. Wang, C. Han, M. Yan, K. Zhao, X. Xu, W. Ren, Y. Zhao, L. Xu, *Nat. Commun.* **2015**, 6, 7402.
- [30] a) M. K. Gnanamani, G. Jacobs, W. D. Shafer, B. H. Davis, *ChemCatChem* **2017**, 9, 492; b) L. Z. Linganis, G. Jacobs, K. G. Azzam, U. M. Graham, B. H. Davis, D. C. Cronauer, A. J. Kropf, C. L. Marshall, *Appl. Catal., A* **2011**, 394, 105.
- [31] a) S. de Carolis, J. L. Pascual, L. G. M. Pettersson, M. Baudin, M. Wójcik, K. Hermansson, A. E. C. Palmqvist, M. Muhammed, *J. Phys. Chem. B* **1999**, 103, 7627; b) M. Yan, T. Mori, J. Zou, F. Ye, D. R. Ou, J. Drennan, *Acta Mater.* **2009**, 57, 722.
- [32] a) K. Yamashita, K. V. Ramanujachary, M. Greenblatt, *Solid State Ionics* **1995**, 81, 53; b) S. Banerjee, P. S. Devi, *Solid State Ionics* **2008**, 179, 661.
- [33] P. Hu, Y. Duan, D. Hu, B. Qin, J. Zhang, Q. Wang, Z. Liu, G. Cui, L. Chen, *ACS Appl. Mater. Interfaces* **2015**, 7, 4720.
- [34] a) K. K. Fu, Y. Gong, J. Dai, A. Gong, X. Han, Y. Yao, C. Wang, Y. Wang, Y. Chen, C. Yan, *Proc. Natl. Acad. Sci. USA* **2016**, 113, 7094; b) D. Lin, P. Y. Yuen, Y. Liu, W. Liu, N. Liu, R. H. Dauskardt, Y. Cui, *Adv. Mater.* **2018**, 30, 1802661.
- [35] a) C. W. Lin, C. L. Hung, M. Venkateswarlu, B. J. Hwang, *J. Power Sources* **2005**, 146, 397; b) W. Liu, S. W. Lee, D. Lin, F. Shi, S. Wang, A. D. Sendek, Y. Cui, *Nat. Energy* **2017**, 2, 17035.
- [36] D. Zhou, R. Liu, Y.-B. He, F. Li, M. Liu, B. Li, Q.-H. Yang, Q. Cai, F. Kang, *Adv. Energy Mater.* **2016**, 6, 1502214.
- [37] Y. Liu, D. Lin, P. Y. Yuen, K. Liu, J. Xie, R. H. Dauskardt, Y. Cui, *Adv. Mater.* **2017**, 29, 1605531.
- [38] Z. Wang, X. Huang, L. Chen, *Electrochem. Solid-State Lett.* **2003**, 6, E40.
- [39] a) F. Capuano, F. Croce, B. Scrosati, *J. Electrochem. Soc.* **1991**, 138, 1918; b) C.-W. Nan, L. Fan, Y. Lin, Q. Cai, *Phys. Rev. Lett.* **2003**, 91, 266104.
- [40] W. Wieczorek, J. Stevens, Z. Florjańczyk, *Solid State Ionics* **1996**, 85, 67.

- [41] a) S. Wen, T. Richardson, D. Ghantous, K. Striebel, P. Ross, E. Cairns, *J. Electroanal. Chem.* **1996**, 408, 113; b) C.-W. Liew, S. Ramesh, R. Durairaj, *J. Mater. Res.* **2012**, 27, 2996.
- [42] V. Ramasamy, V. Mohana, V. Rajendran, *OpenNano* **2018**, 3, 38.
- [43] L. Liu, C. Zheng, J. Wang, Y. Zhang, X. Gao, K. Cen, *Aerosol Air Qual. Res.* **2018**, 18, 1080.
- [44] H. Xu, P.-H. Chien, J. Shi, Y. Li, N. Wu, Y. Liu, Y.-Y. Hu, J. B. Goodenough, *Proc. Natl. Acad. Sci. USA* **2019**, 116, 18815.
- [45] X. Yang, Q. Sun, C. Zhao, X. Gao, K. R. Adair, Y. Liu, J. Luo, X. Lin, J. Liang, H. Huang, L. Zhang, R. Yang, S. Lu, R. Li, X. Sun, *Nano Energy* **2019**, 61, 567.
- [46] a) Y. Xia, T. Fujieda, K. Tatsumi, P. P. Prosini, T. Sakai, *J. Power Sources* **2001**, 92, 234; b) J. Ma, Z. Liu, B. Chen, L. Wang, L. Yue, H. Liu, J. Zhang, Z. Liu, G. Cui, *J. Electrochem. Soc.* **2017**, 164, A3454; c) W. Zhou, Z. Wang, Y. Pu, Y. Li, S. Xin, X. Li, J. Chen, J. B. Goodenough, *Adv. Mater.* **2019**, 0, 1805574.
- [47] J. Chai, Z. Liu, J. Ma, J. Wang, X. Liu, H. Liu, J. Zhang, G. Cui, L. J. A. S. Chen, *Adv. Sci.* **2017**, 4, 1600377.
- [48] J. Evans, C. A. Vincent, P. G. Bruce, *Polymer* **1987**, 28, 2324.
- [49] E. Cockayne, I. Levin, H. Wu, A. Llobet, *Phys. Rev. B* **2013**, 87, 184413.